01 Jan 2024

High-Capacity Anode for Sodium-Ion Batteries using Hard Carbons Derived from Polyurea-Cross-Linked Silica Xerogel Powders

Santhoshkumar Sundaramoorthy

Rushi U. Soni

Stephen Yaw Owusu

Sutapa Bhattacharya

et. al. For a complete list of authors, see *https://scholarsmine.mst.edu/chem_facwork/4028*

Article

High-Capacity Anode for Sodium-Ion Batteries Using Hard Carbons Derived from Polyurea-Cross-Linked Silica Xerogel Powders

Santhoshkumar Sundaramoorthy,[†] Rushi U. Soni,[†] Stephen Yaw Owusu,[†] Sutapa Bhattacharya,
A. B. M. Shaheen ud Doulah, Vaibhav A. Edlabadkar, Chariklia Sotiriou-Leventis,*
and Amitava Choudhury*

Cite This: https://doi.org/10.1021/acsaem.4c01769

Read Online

ACCESS | 📊 Metrics & More | 📖 Article Recommendations | 🔘 Supporting Information

ABSTRACT: In this article, we demonstrated carbon aerogel-silica composites derived from polyurea-cross-linked silica xerogel powders (C-PUA@silica) as anodes for Na-ion batteries. These xerogel-derived hard carbons with embedded silica showed a stable high capacity. Of the several hard carbon samples derived at different temperatures, the pyrolyzed sample at 800 °C (C-PUA@silica-800) showed a high capacity of 236 mAh/g at a current density of 10 mA/g and a stable cycle-life at 200 mAh/g. The galvanostatic charge−discharge curves displayed a sloping voltage profile reminiscent of the adsorption mechanism of Na$^+$ storage. On the other hand, higher temperature-pyrolyzed samples at 1300 °C (C-PUA@silica-1300) displayed a lower capacity of 185 mAh/g at a current density of 10 mA/g, and the charge−discharge profile showed a two-step process, a sloping adsorption mechanism at higher voltage and a flat plateau at lower voltage due to the pore-filling mechanism. The two different types of mechanisms in the two xerogel-derived hard carbons can be attributed to the chemistry and size distribution of pores. The stable cycle life for the C-PUA@silica-800 sample has been attributed to the presence of finely distributed embedded amorphous silica particles, as proven by comparing its performance with hard carbon made without embedded SiO$_2$. These xerogel-derived hard carbons have good electronic conductivity, and the anode can be fabricated without the use of added conductive carbon.

KEYWORDS: anode, sodium-ion batteries, carbon aerogel, polyurea-cross-linked, hard carbon
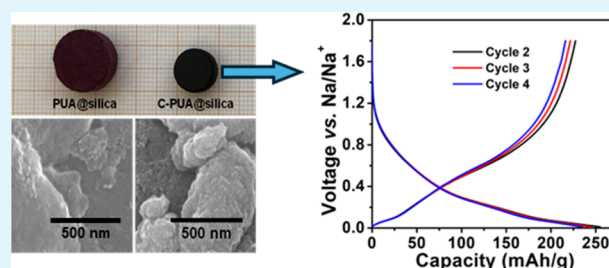
1. INTRODUCTION

The high energy density and cycling stability of rechargeable lithium-ion batteries have revolutionized our modern civilization through successful implementation in portable devices and electric vehicles.[1] However, the low natural abundance (∼0.01%) and nonuniform distribution of lithium in the Earth's crust are soon going to be an impediment for large-scale energy storage applications.[2] Therefore, to sustain the development on electrification of our vehicles and other large-scale stationary energy storage applications, low-cost and widely available energy storage technologies are much sought after.[3] Among different energy storage technologies, sodium-ion batteries (NIBs) hold the greatest potential as the natural abundance of sodium is very high and the commercialization of NIB technology is on the horizon.[3,4] As of today, a large number of NIB cathodes have been discovered[5]; however, the absence of a suitable anode is the greatest bottleneck toward commercialization of NIBs.[5] Carbonaceous anodes, particularly hard carbon-based materials, show promising properties for practical use.[6,7] Since the discovery by Dahn and Stevens,[8,9] the hard carbons are currently being extensively investigated to improve their performance and understand the mechanism of Na storage in hard carbon.[6−12] In this respect, different

strategies are adopted to create hard carbon with higher capacities and cycling stability and improve the low initial Coulombic efficiencies (ICEs).[13−21] These strategies include the use of new precursors,[21] controlling the microstructures (surface defects, porosity: open vs closed pores, surface area)[11,15,18,22] and heteroatom doping by employing innovative synthetic techniques.[17,23−25] For hard carbon, a broad range of precursors, including resin-based [e.g., phenolic (phenol-formaldehyde), epoxy, polyaniline, polyacrylonitrile (PAN), etc.],[13,25−29] biomass-based (e.g., lignocellulosic, corn cobs, etc.),[20,30−36] and polymer/plastic-based (e.g., polystyrene, polyethylene terephthalate, etc.), have been used.[37−39] These precursors are often cross-linked or subject to cross-linking via pyrolysis at higher temperatures. Another well-known family of cross-linked 3-D carbon network structures is carbon aerogels.

Scheme 1. Synthesis of Silica-Embedded Carbon Aerogel through the Aerogel-via-Xerogel Route
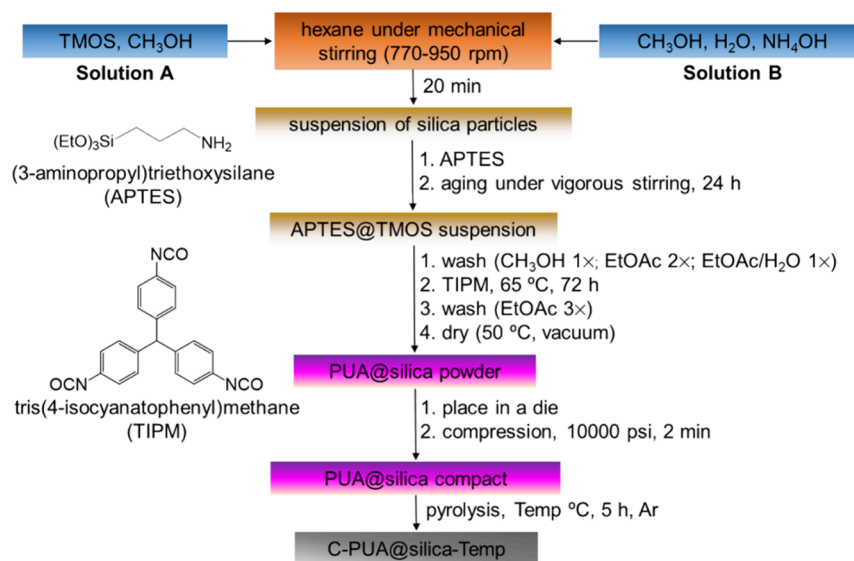
The carbon aerogels can be derived from organic polymeric aerogels based on phenolic resins (e.g., phenol, resorcinol, phloroglucinol, cresol in combination with an aldehyde), aromatic polyureas, polyamides, polyimides, PAN, polybenzoxazines, etc., through high-temperature pyrolysis.[40−43] The properties of carbon aerogels can be tuned by choosing the appropriate precursors, synthetic conditions, and pyrolysis temperatures.[44] The interconnected primary particles are responsible for the 3D network, and the nature of microporosity is a function of intraparticle architectures. On the other hand, the interparticle morphology guides the formation of mesopores and macropores.[44] The ability to tailor the development of micro- and mesopores independent of each other in the carbon aerogel brings about a unique opportunity for applications, especially in Na-ion anodes. However, this unique potential of carbon aerogels has not been exploited to develop Na-ion anodes, except for one or two cases.[45,46] Motivated by this versatility and tunability, we investigated the carbon aerogel-silica composites derived from polyurea-cross-linked silica xerogel powders as anodes for NIBs. In this article, we demonstrated that xerogel-derived hard carbons with embedded silica show stable high capacity for Na-ion anodes.

2. EXPERIMENTAL SECTION

2.1. Materials. All reagents and solvents were used as received, unless noted otherwise. Ammonium hydroxide (NH$_4$OH, ACS reagent) and (3-aminopropyl)triethoxysilane (APTES) were purchased from Fisher Scientific. Tetramethylorthosilicate (TMOS) was purchased from Sigma-Aldrich Chemical Co. HPLC grade solvents, including hexane, methanol (CH$_3$OH), and ethyl acetate (EtOAc), were purchased from Fisher Scientific. Technical grade acetone was purchased from Univar (St. Louis, MO). Tris(4-isocyanatophenyl)-methane) (TIPM) was donated by Covestro LLC (Pittsburgh, PA) as a 27% w/w solution in dry EtOAc under the trade name Desmodur RE. Ultra-high-purity Ar (grade 5) and N$_2$ (grade 4.8) gases were purchased from Airgas (Rolla, MO).

The sections below present the preparation, chemical transformations, and characterization data of various intermediates, along with their processing conditions.

2.2. Preparation of PUA@Silica Xerogels and Aerogels.
2.2.1. Synthesis of PUA@Silica Xerogels. The overall process for the preparation of porous carbon aerogels is summarized in Scheme 1. The synthesis of carbon aerogels by the aerogel-via-xerogel method

was carried out with a carbonizable aromatic polyurea (PUA), following the procedure described by Soni et al.[47] In this method, the sol−gel silica skeleton was obtained by mixing solution A (TMOS in methanol) and solution B (NH$_4$OH + water in methanol),[48] followed by adding the combined mixture in hexane under vigorous mechanical stirring.[49] During the progress of the reaction, suspended silica particles turned the continuous phase of hexane into a milky white. APTES was added to the silica suspension at a 4:1 mol/mol ratio of TMOS/APTES. In this way, APTES was attached to silica primary particles. The APTES@silica hexane suspension was aged at room temperature for 24 h. The white milky suspension was further washed once with methanol, followed by washing twice with ethyl acetate and once with a 1:1 (v/v) solution of ethyl acetate/water. TIPM, a carbonizable polymer source, was added as a mixture of 37% TIPM solution of ethyl acetate (commercially known as Desmodur RE), and the reaction mixture was kept at 65 °C for 72 h, where TIPM forms polyurea after cross-linking with the dangling −NH$_2$ group of APTES attached with silica particles.[50] The concentration of TIPM was kept at a 4.5× mol/mol ratio of silicon in APTES@silica. The resulting wet silica solution was washed with ethyl acetate and dried at 50 °C under vacuum to obtain a free-flowing xerogel powder. This powder is termed PUA@silica powder.

2.2.2. Processing of PUA@Silica Xerogels into Carbon Aerogels. Dry PUA@silica powders were placed in suitable dies and were compressed with a hydraulic press at 10,000 psi for 2 min to form PUA@silica disks (Scheme 1). The carbonization of PUA@silica disks was carried out by direct heating at 800 °C under an inert gas flow (Ar) for 5 h. They are referred to as C-PUA@silica-800. Similarly, 1000, 1300, and 1500 °C carbonized samples were referred to as C-PUA@silica-1000, C-PUA@silica-1300, and C-PUA@silica-1500, respectively.

2.3. Methods. *2.3.1. Pyrolytic Carbonization of PUA@Silica Compacts.* Pyrolytic carbonization of PUA@silica compacts to C-PUA@silica compacts was carried out in a programmable MTI GSL1600X-80 tube furnace. The rate of heating and cooling was always maintained at 2.5 °C min^{-1}. All gas flow rates were set at 325 mL min^{-1}.

2.3.2. Characterization of the Aerogels. 2.3.2.1. Physical Characterization. Skeletal densities (ρ_s) were measured by helium pycnometry on a Micromeritics AccuPyc II 1340 instrument. Samples for skeletal density measurements were outgassed for 24 h at 80 °C under vacuum before analysis. Percent porosities (Π) were determined from the ρ_b and ρ_s values via Π = 100 × [(ρ_s−ρ_b)/ ρ_s].

2.3.2.2. XPS. X-ray photoelectron spectroscopic analysis (XPS) was carried out with a ThermoFischer Scientific Nexsa X-ray Photoelectron Spectrometer System. Samples were mixed and ground
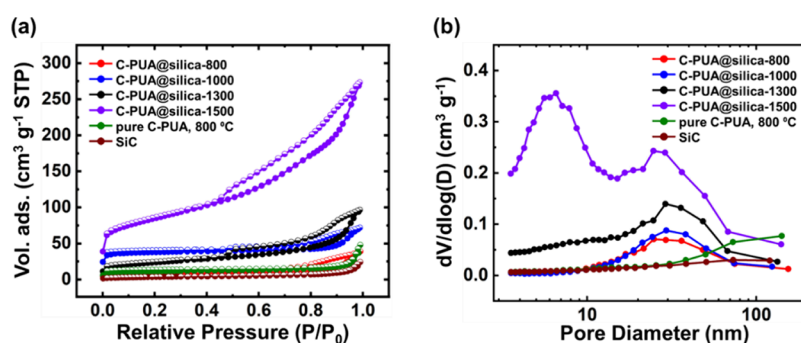
Figure 1. (a) BET surface area plot and (b) BJH pore size distribution.

Table 1. Material Characteristics of Silica-Embedded Carbon Aerogels at Different Pyrolysis Temperatures and Comparison with Pure PUA-Based Carbon and SiC

sample	skeletal density, ρ_s [g cm^{-3}][a]	bulk density, ρ_b [g cm^{-3}][b]	BET surface area, σ [m^2 g^{-1}][c]	pore volume [m^2 g^{-1}]		average pore diameter, [nm]			average particle diameter, [nm][i]
				$V_{1.7-300nm}$[d]	V_{max}[e]	from $V_{1.7-300nm}$[f]	from V_{max}[g]	from BJH plot[h]	
C-PUA@silica-800	1.901 ± 0.011	0.937 ± 0.014	24.74 (10.71)	0.05	0.06	9.2	9.7	24.8	127.6
C-PUA@silica-1000	1.983 ± 0.030	[j]	114.43 (93.69)	0.06	0.11	2.1	3.9	29.4	26.4
C-PUA@silica-1300	2.334 ± 0.048	[j]	80.82 (18.84)	0.14	0.15	6.9	7.4	29.0	31.8
C-PUA@silica-1500	2.597 ± 0.061	[j]	228.12 (74.62)	0.36	0.42	5.1	5.9	6.5, 29.6	8.0
pure C-PUA, 800 °C	1.952 ± 0.026	[j]	34.59 (17.22)	0.06	0.07	6.4	8.5	141.6	88.9
pure SiC	3.189 ± 0.088	[j]	12.47 (1.59)	0.03	0.04	10.9	12.0	120.0	150.9

[a]Single sample, average of 50 measurements. [b]Average of three samples. [c]Surface area calculated from N_2 sorption via BET theory, numbers in (parentheses): micropore surface area calculated via the t-plot method. [d]$V_{1.7-300nm}$ was calculated via the BJH desorption cumulative pore volume. [e]V_{max} was calculated via a single-point maximum adsorption method from N_2 adsorbed at 77K as P/P_0 approaches zero. [f]Average pore diameters were calculated via the $4 \times V/\sigma$ method by using $V_{1.7-300nm}$. [g]Average pore diameters were calculated via the $4 \times V/\sigma$ method by using V_{max}. [h]Measured from N_2-sorption BJH pore size distribution (Figure 1b). [i]Average particle diameters were calculated via the $6/\rho_s \times \sigma$ method. [j]These experimental bulk densities could not be obtained because the samples were obtained as powders.

together with Au powder (5 wt %) as an internal reference. Deconvolution of the spectra was performed with Gaussian function fitting by using the OriginPro 9.7 software package.

2.3.2.3. Structural Characterization. SEM and TEM. Scanning electron microscopy (SEM) and energy-dispersive X-ray spectroscopy were conducted with Au/Pd (60/40)-coated samples on a Hitachi Model S-4700 field-emission microscope. Samples were placed on the stub using a C-dot. Thin sticky copper strips were cut and placed on the edges and top of the sample, leaving space for the analysis. Digital photographs of a typical PUA@silica disk, its carbonized version (800 °C), and the corresponding SEM images are given in the SI (Figure S1). As can be seen from the photographs, there is considerable shrinkage in the volume of the disk due to the loss of organic components. The SEM images do not contain any significant feature, except that there is a sign of surface roughness after carbonization. The microstructure of the carbonized samples was characterized by transmission electron microscopy (TEM).

2.3.2.4. BET Surface Area and Pore Structure Analysis. The pore structure was probed by N_2-sorption porosimetry at 77 K using either a Micromeritics ASAP 2020 or a TriStar II 3020 surface area and porosimetry analyzer. Before porosimetry, samples were outgassed for 24 h under a vacuum at 120 °C. Data were reduced to standard conditions of temperature and pressure. Total surface areas were determined via the Brunauer–Emmett–Teller (BET) method from the N_2-sorption isotherms. Micropore analysis was conducted with low-pressure N_2 sorption at 77 K by using a Micromeritics ASAP 2020 instrument equipped with a low-pressure transducer. Pore size distributions were determined by the Barrett–Joyner–Halenda (BJH) equation applied to the desorption branch of the N_2-sorption isotherms.

2.3.2.5. FTIR. Powdered samples of C-PUA@silica-Temp were used for FTIR measurements in a Thermo Nicolet iS50 FT-IR spectrometer in ATR mode for a wavenumber range of 400–4000

cm^{-1}. OMNIC software was used for data acquisition and data analysis.

2.3.2.6. RAMAN. Raman spectroscopy was conducted with an XplorA Plus Confocal Raman Microscope equipped with an air-cooled 532 nm solid-state100 mW laser and a TE air-cooled CCD detector (Horiba Instruments, Inc., Piscataway, New Jersey).

2.3.3. Fabrication of Na-Ion Cell. The working electrode composition was prepared with C-PUA@silica-Temp, SiO_2, and SiC samples as the active materials along with carbon black and poly(vinylidene fluoride) (PVDF) in a ratio of 75:15:10. PVDF was predissolved in *N*-methyl-2-pyrrolidone (NMP) (0.0444 g/mL NMP) to form the slurry. Initially, the active material and the conducting carbon were ball-milled for 20 min, followed by the addition of PVDF dissolved in NMP, and ball-milled for another 10 min to form the slurry. The slurry was then coated on the Cu foil and dried under vacuum at 80 °C for 12 h. In order to evaluate the intrinsic electronic conductivity of the material, C-PUA@silica-800 was chosen to prepare a conductive carbon free electrode with an active mass to PVDF ratio of 90:10. Finally, the electrodes were cut into a disk shape with an active mass loading of ∼1 to 2 mg (which is equivalent to 0.00140−0.00280 g/cm²). All the cell fabrications were carried out in a glovebox under an argon atmosphere (O_2 < 0.1 ppm and H_2O < 0.1 ppm). The electrochemical evaluations were carried out in CR2032-type coin cells with Na metal as counter and reference electrodes, 1 M $NaClO_4$ in an ethylene carbonate/dimethyl carbonate (1:1) solution as the electrolyte, and Whatman glass fibers as the separator. All of the galvanostatic measurements were done using a Neware battery tester at different current rates ranging from 10 to 200 mA/g. The specific capacity of the carbon materials was calculated based on the mass loading of the active material in the electrode. Cyclic voltammetry was carried out in an EG&G PAR 273 potentiostat at a scan rate of 50 μV/s.

C

3. RESULTS AND DISCUSSION

3.1. Surface Area and Pore Size Distribution. The N_2-sorption isotherms of C-PUA@silica-Temp samples as a function of the temperature of carbonization and BJH analysis of the desorption traces of the isotherms of all samples are given in Figure 1a,b, respectively. The nitrogen adsorption–desorption isotherms of C-PUA@silica-Temp samples can broadly be classified as type IV isotherms with type H3 hysteresis loops. Type IV signifies that the materials are mesoporous, and the adsorption takes place via multilayer adsorption, followed by capillary condensation in mesopores and restrictive uptake at higher P/P_0, thus creating a hysteresis loop. On the other hand, H3 hysteresis indicates that slit-like openings are formed by the aggregation of particles. The comprehensive characterization data of materials are listed in Table 1.

3.2. Powder X-ray Diffraction. To investigate the nature of carbon and formation of other crystalline products as a function of pyrolysis temperature, powder X-ray diffraction (PXRD) was carried out. XRD of all of the pyrolyzed silica-embedded carbon aerogels revealed that there was no SiC present in the 800 and 1000 °C carbon aerogels. In the case of 1500 °C carbon aerogels, sharp identification diffraction lines of β-SiC from the (111), (220), and (311) planes were present (Figure 2). Most importantly, PXRD of C-PUA@silica-800
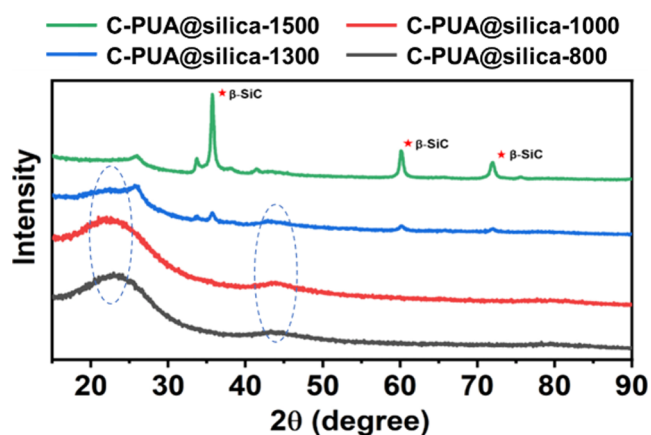
Figure 2. PXRD of porous silica-embedded carbon aerogels.

and -1000 clearly exhibited broad lines centered at $2\Theta = \sim22$ to 23° and 43°, corresponding to the (002) and (100) lines of graphite, indicating strong evidence of hard carbon formation. The loss of graphitization is reflected by the shift of the (002) line to a low angle and the broadening of the peak, signifying an increase in the interlayer spacings from 0.34 to 0.45 nm and a lack of ordering, respectively. As the temperature of carbonization increased beyond 1000 °C, there was an emergence of a more graphite-like sharp peak at $2\Theta = \sim26°$ ($d_{spacing} = 0.34$ nm), along with the formation of β-SiC, due to the carbothermal reduction of SiO_2 to SiC.[49,51]

3.3. XPS Analysis. The effect of carbonization temperature on the surface oxygen and nitrogen functional groups is studied by XPS. It is very important to know the presence of various heteroatoms and the functional groups to which they belong since these heteroatoms play a pivotal role in the mechanism of Na uptake in hard carbon. Figure 3 shows the fitted C, N, and O 1s and Si 2p XPS spectra of the carbonized PUA aerogels at different temperatures, and the atomic percentage of each

element from the deconvoluted XPS spectra is given in Table S1. It can be noted that all the fitted O 1s XPS spectra contain Si–O at ~533.00 eV and C–O at ~533.5 eV.[47] The C–O exists in the phenoxide of C-PUA. The peak at 533.0 eV indicates the presence of silicate oxygen, the percentage of which decreases at the 1500 °C sample due to the formation of SiC, thereby showing almost equal amounts of C–O and Si–O. A peak at 103.6 eV due to Si 2p conclusively proves the presence of SiO_2 in all samples. Besides the presence of SiO_2, the Si 2p peak at 101 eV for 1300 and 1500 °C pyrolyzed samples proves the presence of SiC in the sample due to the carbothermal reduction of SiO_2 to SiC.[52] On the other hand, peaks in N 1s spectra can be deconvoluted into two major groups: one centered at 398.4 eV due to pyridinic nitrogen and another centered at 400.7 eV can be assigned to para-hydroxy pyridinic (pyridonic) nitrogen besides a small fraction of pyridine-N-oxide at ~402.8 eV, especially at low-temperature-pyrolyzed samples. With the increasing temperature of pyrolysis, the percentage of pyridinic N decreases; however, the percentage of pyridonic N remains almost constant. The C 1s spectra as a function of temperature of pyrolysis yield valuable information about the presence of heteroatoms and the development of aromatic carbon. As seen in the 800 °C sample, the signature of the functional groups, C=N (285.3 eV) and C=O (287.2 eV), still exist at higher temperature-pyrolyzed samples, as also seen in N and O 1s spectra, along with the presence of aromatic carbon at 284.7 eV. With increasing temperature, the percentage of aromatic C increases, as also evident in the PXRD; however, the signature of functional groups (heteroatom-bound carbon) still exists, especially the signature of C=N remains around the same percentage at all temperatures of pyrolysis. This shows that even after increasing the carbonization temperature, the adsorption sites for Na^+ still remain. Nonetheless, at very high carbonization temperatures (1500 °C), a reduction in the adsorption sites occurs, as seen in the decrease of C=O content for C-PUA@silica-1500.

3.4. IR Spectra. IR spectra of all the samples, as given in Figure S2, show Si–O–Si rocking vibration at 460 cm^{-1}, Si–O bending at 815 cm^{-1}, and O–Si–O asymmetric stretching modes at 1025 cm^{-1}. The increase in the intensity of peaks in the C-PUA@silica-1500 sample indicates the presence of Si–O and Si–C bond deformation at 880 cm^{-1}. This is due to the wide absorption spectrum of SiOC between 1100 and 800 cm^{-1}.[46,53]

3.5. Raman Analysis. All samples for the Raman experiments were first degassed with flowing nitrogen. The analysis was conducted with a laser power set at 1% of its maximum and 15 s of accumulation time elapsed, and a total of 16 scans were taken and averaged. Using these conditions prevented the background spectra from getting intensified and drifting upward.[54] They also enabled well-resolved bands to be acquired. With increasing carbonization temperatures, graphitization of the carbon aerogel increases, and silica reacts with the carbon aerogel to form SiC.[49] The presence of a graphitic carbon phase and SiC formation was confirmed by Raman acquisitions on carbonized samples. The unfitted raw spectra are given in the SI (Figure S3). The Raman spectra of the samples display D and G bands, corresponding to disordered/defective carbon and graphitic structures, respectively (Figure 4). The fitting of the Raman spectra include D and G bands at 1370 and 1590 cm^{-1}, respectively, along with smaller peaks at T and D″ attributed to amorphous carbon/impurities/
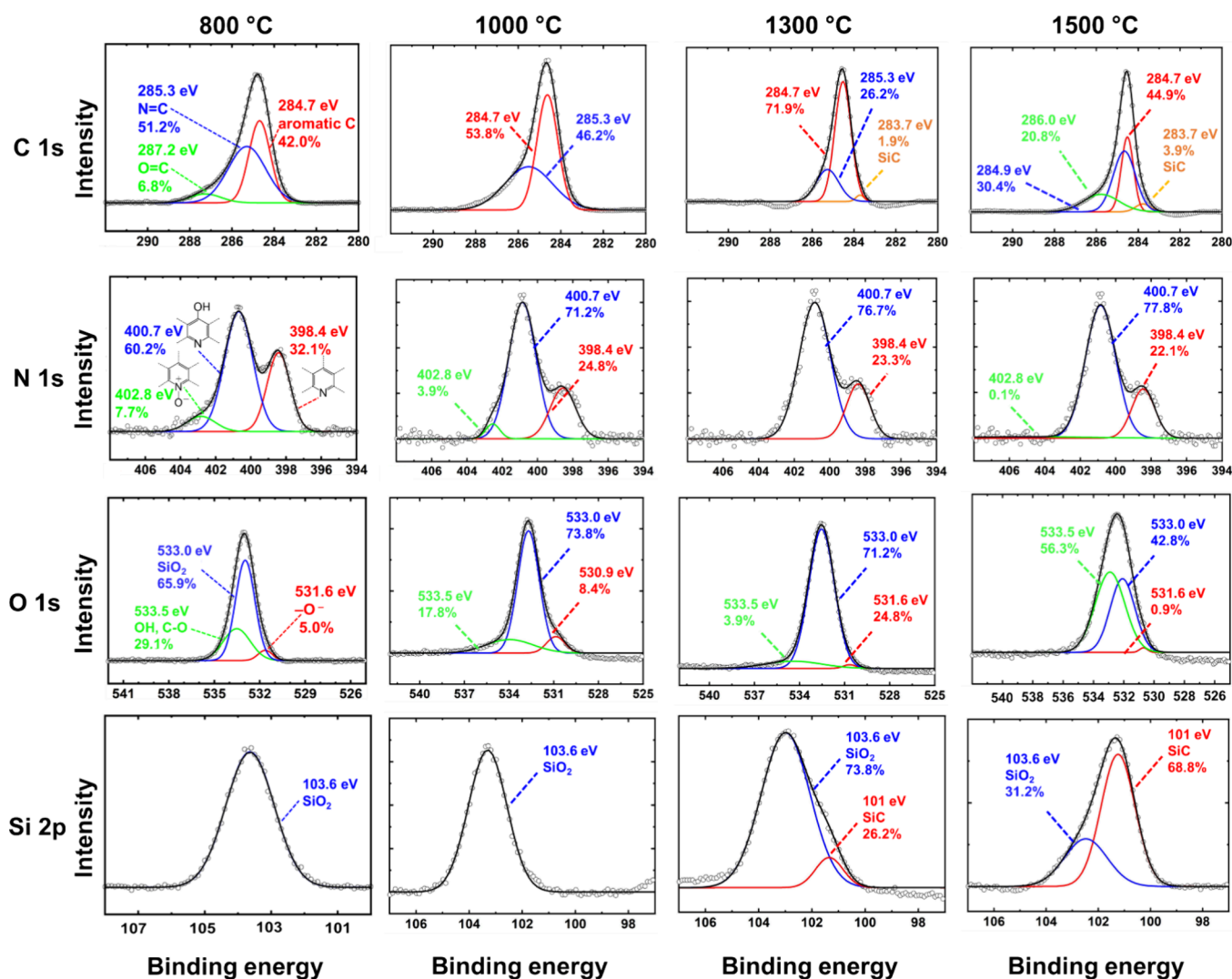
Figure 3. High-resolution C, N, and O 1s and Si 2p XPS spectra of C-PUA@silica at 800, 1000, 1300, and 1500 °C.
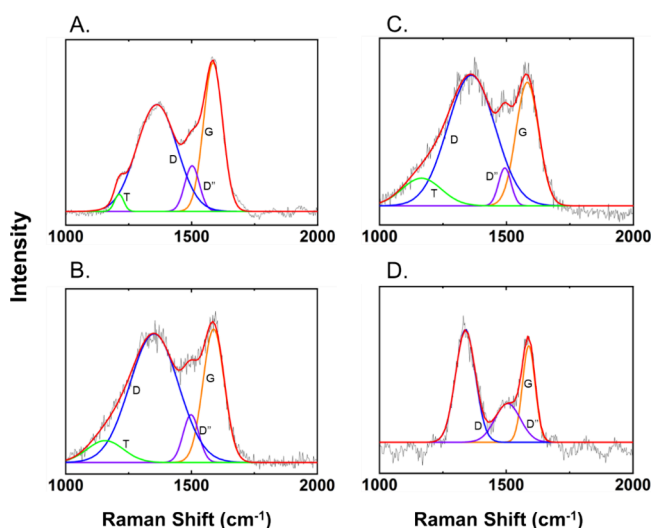
Figure 4. Fitted Raman spectra of C-PUA@silica aerogels carbonized at 800 °C (A), 1000 °C (B), 1300 °C (C), and 1500 °C (D).

heteroatoms and defects (1235 and 1490 cm^{-1}), respectively.[24,46,55] The intensity ratio of D and G peaks from the fitted spectra (I_D/I_G) can be utilized to evaluate the amount of

defects and graphitic carbon as a function of the temperature of carbonization. It can be seen that the ratio of I_D/I_G increases (Table S2) as a function of temperature from 800 to 1500 °C samples, clearly indicating an increased degree of graphitization with increasing carbonization temperatures. This also implies that hard carbon obtained at 800 °C (C-PUA@silica-800) with more defects, heteroatoms, and less ordered graphitic layers would be a good candidate for Na-ion anodes. Besides these fitted peaks, the Raman spectra contain a broad peak centered at ∼3000 cm^{-1} due to the overtones of the main peaks and a sharp peak at 799 cm^{-1} for C-PUA@silica-1500 due to β-SiC. Another signature peak for β-SiC at ∼970 cm^{-1} is barely seen due to defects in β-SiC (Figure S3).[56,57]

3.6. TEM. To evaluate the microstructural changes of hard carbons during the carbonization processes at different temperatures, TEM analysis was carried out for two samples, C-PUA@silica-800 and -1500 (Figure 5). The low-resolution TEM images of Figure 5 (top panel) show the presence of a carbonaceous matrix somewhat disordered in nature. The lattice fringes with higher interlayer spacings could not be resolved due to limitations in our microscope. On the other hand, the low-resolution TEM images of the 1500 °C sample clearly show contrasting images of needle-shaped SiC in the carbonaceous matrix. On higher resolution, the lattice fringes
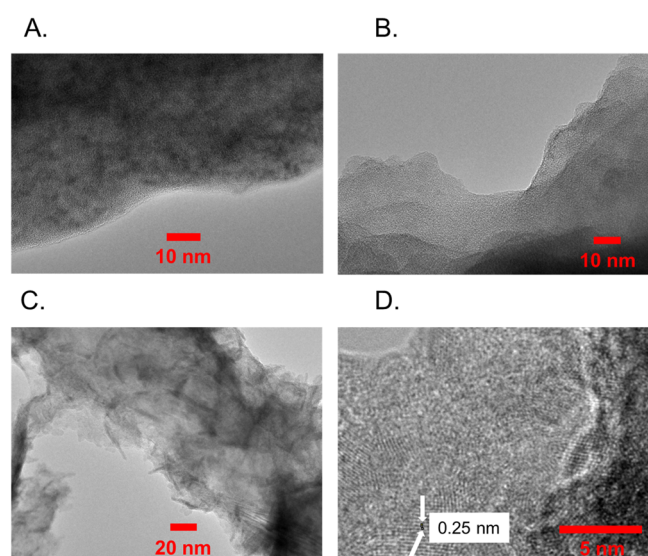
Figure 5. TEM images of C-PUA@silica hard carbon pyrolyzed at 800 (A, B) and 1500 °C (C, D). Inserted arrows represent the interlayer distances of β-SiC.

for SiC can be resolved and a separation of 0.25 nm can be attributed to the (111) planes of β-SiC (Figure 5, bottom panel).[52]

3.7. Electrochemical Analysis. The electrochemical investigation of Na^+ storage was carried out in a half-cell configuration with Na metal as the reference and counter electrodes. The upper and lower cutoff regions were set at 1.8 and 0.01 V, respectively, against Na/Na^+ in all of the electrochemical tests, unless otherwise mentioned. Galvanostatic charge−discharge (GCD) profiles of the hard carbons tested at a 10 mA/g current density are presented in Figure 6. Among all the samples, C-PUA@silica-800 shows a maximum

capacity of 236 mAh/g with an ICE of 38%. In the open-pore carbon systems, the increase in the synthesis temperature will result in a drastic surge of the surface area with the removal of carbon and a reduction in particle size with a note of caution that heating time and rate can also have an influence. This results in the formation of a larger solid−electrolyte interface (SEI), and hence the low ICE. Having SiO_2 in the open-pore system helps to minimize the degree of surface area changes. It is evident from the BET surface area that PUA with SiO_2 (C-PUA@silica-800) has a lower surface area (24.74 m^2/g) compared to PUA without SiO_2 (34.59 m^2/g) under a similar synthesis temperature, for example, at 800 °C (see Table 1). Though the surface area increased while moving from 800 to 1300 °C, the ICE also improved by ∼7%, followed by a drop at 1500 °C (Figure S4a) due to the creation of smaller pore (open) diameters at high temperatures, as one can see in the BJH bimodal pore-size distribution in C-PUA@silica-1500, showing one-distribution with a smaller mean diameter of 6.5 nm (Figure 1b and Table 1). During the subsequent cycle, the ICE improved to ∼92% and eventually reached 98% in all C-PUA@silica-Temp samples owing to the stable SEI formation. The GCD plot of the C-PUA@silica-800 sample has only a sloping voltage profile until the lower cutoff region, suggesting that the Na^+ storage mechanism is exclusively due to adsorption behavior, as also seen in some previous studies.[7,10−12] Also, the XPS revealed the presence of more functional groups in the low-temperature (800 °C) carbonized materials, facilitating the Na^+ adsorption sites. Due to the sloping profile, the nominal voltage achieved by C-PUA@silica-800 was 0.4 V. Unlike C-PUA@silica-800, the GCD profiles of C-PUA@silica-1000, -1300, and -1500 samples can be separated into two distinct regions. A sloping profile until 0.14 V, followed by a plateau profile in the lower voltage region. As the contribution of capacity from the plateau region increased, the nominal cell voltage of each material reduced
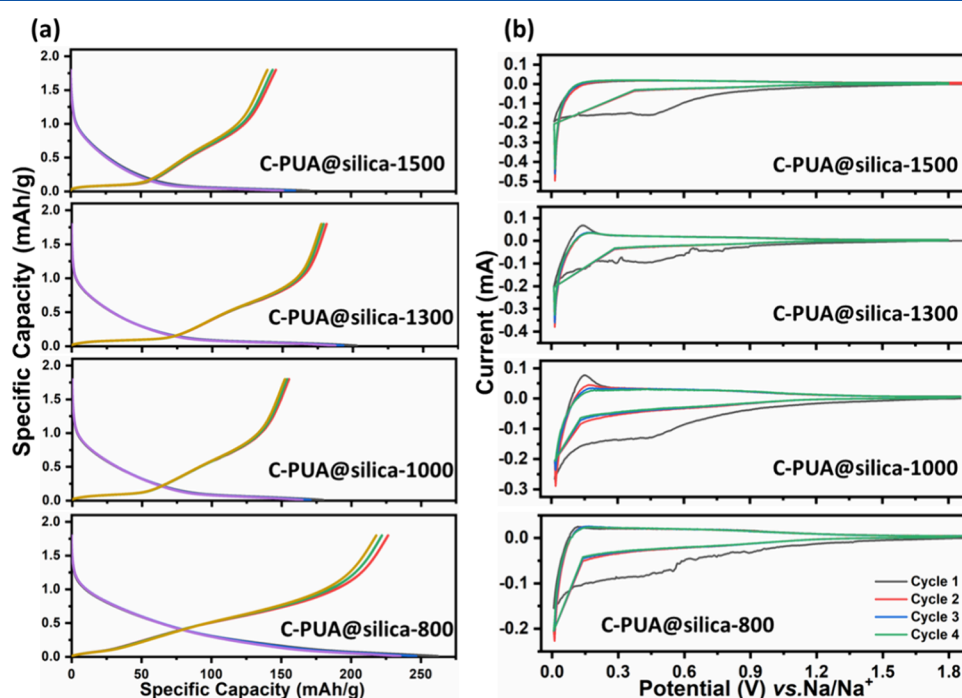
Figure 6. (a) Charge−discharge profile of C-PUA@silica-800, -1000, -1300, and -1500 samples (red, green, and yellow traces represent 2nd, 3rd and 4th discharge cycles, respectively) and (b) cyclic voltammogram of C-PUA@silica-800, -1000, -1300, and -1500 samples.
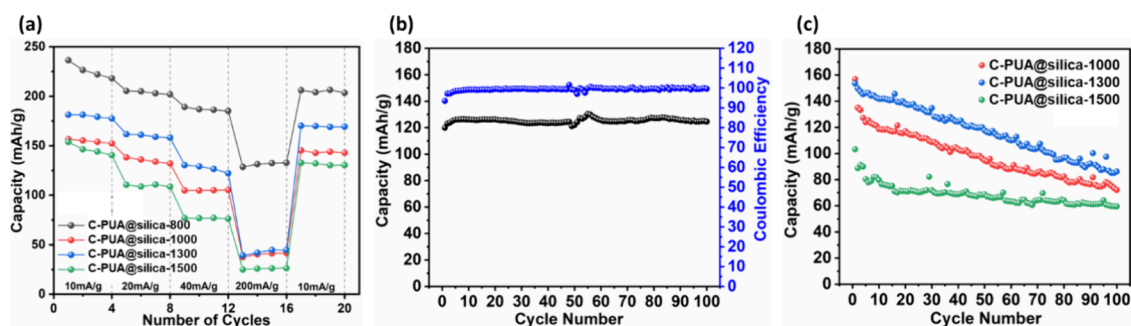
Figure 7. Electrochemical test done on C-PUA@silica carbonized at different temperatures. (a) Rate performance at different current densities, (b) long cycle at a 200 mA/g current density for C-PUA@silica-800, and (c) long cycle at a 40 mA/g current density for C-PUA@silica-1000, -1300, and -1500 samples.

drastically (Figure S4b). We believe that the capacity contribution from the low-voltage region can be ascribed to the pore-filling mechanism. The capacity gain from the plateau region progressively increased because of the changing chemistry of the pores, such as a reduction of functional groups and an increase of graphitic carbon, as well as physical reasons, such as a decrease in pore diameter (Table 1). Though BJH pore size distribution (mean diameter) did not show any trend, employing the $4 \times V/\sigma$ method by using volume (V) as $V_{1.7-300nm}$ (where $V_{1.7-300nm}$ refers to the cumulative volume of pores of diameter between 1.7 and 300 nm) or V_{max} (Table 1), we do see a decrease of average pore diameters at high-temperature carbonized samples.

In porous systems, it is seen that the pore volumes, $V_{1.7-300nm}$, increase with increasing temperature (Table 1). Also, it is to be noted that the pore sizes are larger in C-PUA@silica-800 (9.7 nm), while they are gradually reduced to 7.4 nm at C-PUA@silica-1300, making the pore sizes more optimum for Na$^+$ to access. While moving to C-PUA@silica-1500, the pore size again decreased (5.9 nm), which can be directly observed in the GCD profile with the reduction of the capacity contribution from the plateau region. The decrease of overall capacity in C-PUA@silica-1500 samples can also be attributed to the presence of a substantial amount of electrochemically inactive β-SiC. The cyclic voltammograms (CVs) of the samples show a degree of irreversibility in the first cycle (Figure 6b). An irreversible reduction peak around 0.5 V can be clearly observed in the first charge of each sample due to the decomposition of the electrolyte and the formation of the stable SEI. The smaller the intensity of the reduction peak is, the higher the electrochemical reversibility. The intensity of the reduction peak clearly reduced from C-PUA@silica-800 to -1300, and correspondingly, the ICE also improved in the same manner. In C-PUA@silica-1500, the intensity increased, and at the same time, there was a decrease in the ICE. This suggests that though the surface area increased, the reduction in the pore diameter facilitated the improvement in the reversibility. Also, it is important to note that the area under the first cycle was broad over the voltage region of 1.2−0.01 V, suggesting that the SEI was formed continuously with the consumption of the electrolyte. In the consecutive CV cycles, the irreversible peak disappeared and only a pair of reversible redox peaks were observed near 0.1 V, and the ICE improved to ∼92% in all of the C-PUA@silica-Temp samples. The CV features do not change much with a faster scan rate, as evident by the 0.1 mV/s scan of the PUA@silica-800 cell (Figure S5). The rate capability of the samples was tested with GCD at different

current densities ranging from 10 to 200 mA/g (Figure 7). It can be observed that the capacity of each sample decayed with the increase in the current density (Figure S4c). Out of all carbon aerogel-silica composites, C-PUA@silica-800 has retained ∼120 mAh/g capacity even at a 200 mA/g current density, while the other high-temperature samples showed a capacity of less than ∼50 mAh/g. The stability of the material at a high current rate can be corroborated by the mass ratio of carbon to SiO$_2$. Though SiO$_2$ helps in reducing the degree of surface area changes, it is intrinsically inactive for the electrochemical storage of Na$^+$ (Figure S6). The increase in synthesis temperature induced the loss of carbon from the matrix, resulting in a higher surface area and a low carbon-to-SiO$_2$ ratio. Hence, the high-temperature samples showed low capacity retention at higher current rates due to the presence of more inactive SiO$_2$. On the other hand, during carbonization at elevated temperatures, such as C-PUA@silica-1300 and -1500, SiO$_2$ reacts with the carbon matrix and forms SiC (Figure S6).

The formation of SiC is not beneficial for Na$^+$ storage, as the bulk SiC is also electrochemically inactive (Figure S6c) and adds extra dead mass to the electrode. Not only that, but we also see the emergence of graphite-like peaks in the PXRD of high-temperature carbonized samples, which is again not conducive to Na-ion insertion. As observed from the rate capability curves, it is evident that an optimum level of SiO$_2$ in the carbon matrix can withhold the skeletal structure of the material and enhance the rate capability. In order to evaluate this claim, the C-PUA-800 sample without any SiO$_2$ was subjected to electrochemical evaluations. Due to the absence of SiO$_2$, the surface area increased (∼10 m^2/g greater than C-PUA@silica-800), forming a larger SEI, followed by a severe capacity fade in the initial cycles (Figure S6b). This demonstrates the synergistic effect of SiO$_2$ in the carbon matrix. Further, when the samples were cycled back to low current density, all C-PUA@silica-Temp samples retained more than 90% of their initial capacity, supporting that SiO$_2$ maintains the structural integrity of the carbon matrix (Figure 7a). The long-cycle life test was carried out at a current density of 200 mA/g for C-PUA@silica-800 (Figure 7b), while the rest of the samples were tested at a current density of 40 mA/g (Figure 7c). As expected, after 100 cycles, C-PUA@silica-800 showed excellent cycling stability even at a much higher current rate with ∼98% of the initial capacity retention, while the other samples showed drastic capacity degradation even at a low current rate. These electrochemical tests further reiterated the positive role of SiO$_2$ for the material's stability.

We attribute this synergism to our synthesis techniques, where, in the first step, the finely dispersed silica microparticles from TMOS are surface-modified by anchoring APTES onto them. Subsequently, triisocyanate (TIPM) was attached to APTES@ silica through the dangling −NH$_2$ group of APTES as well as through −OH termination of silica particles (Scheme 2), as it

Scheme 2. Possible Way of Anchoring Polyurea on the Surface of Silica
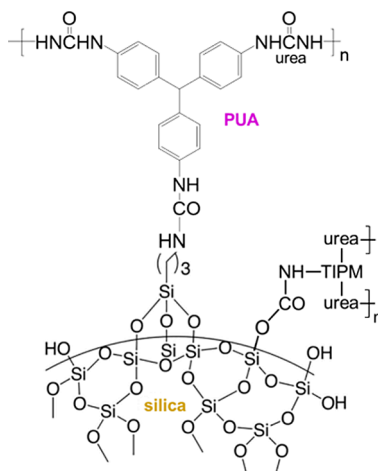
was determined by the solid-state ^{29}Si and ^{13}C CPMAS NMR of polyurea@silica (PUA@silica) and APTES@silica.[47] Since we do not see any signature of crystalline SiO$_2$ in the carbonized samples C-PUA@silica-800 and -1000 samples, it can be said that silica is still separated and well dispersed in the carbon matrix to prevent any agglomeration to form crystalline SiO$_2$ during the redistribution of carbon precursors to form the hard carbon. Our approach is also different from the SiOC-hard carbon composites through the use of a polyorganosilox-ane-type preceramic polymer, where free carbon and silicon-oxy-carbide are separated.[46,53]

Cost reduction and sustainability are the two most important driving factors for the development of modified hard carbon anodes for NIBs. The low cost of polyurea and good electrochemical stability due to the evaporated SiO$_2$ make the C-PUA@silica-Temp samples suitable candidates as anode materials for NIBs. Further, the elimination of conducting carbon in the battery fabrication can provide an added advantage in the view of low cell fabrication cost. All the electrode preparation for alkali-ion batteries involves the addition of a certain amount of conducting carbon to provide the conductivity for the active material and enhance its cyclability at high current rates. In this study, we also demonstrated that the samples are intrinsically conducting enough to be cycled without the use of additional conducting carbon. To prove this, we chose the C-PUA@silica-800 sample, prepared the anode without the addition of conducting carbon, and subjected it to electrochemical tests (Figures 8 and S7). The GCD profile of C-PUA@silica-800-WCC (without conductive carbon) shows exactly the same capacity as C-PUA@silica-800 with a slightly higher ICE of ~46% (Figures 8a and S4c). This is evident from the CV plot (Figure 8b) exhibiting a reduced area under the first cycle. In the consecutive cycles, the reversible reduction and oxidation peak around 0.1 V was also clearly observed. Though there was a slight capacity fade at higher current densities, the sample was able to achieve almost all of its initial capacity while being cycled back to a low current rate (Figure 8c). The cycle life evaluation of C-PUA@silica-800-WCC at a high current rate (200 mA/g) showed an initial capacity retention of 84% without any conducting carbon, which is remarkable. These results open a new avenue for designing hard carbon materials with suitable structure stabilizers to enhance the cyclability at high current rates while minimizing the consumption of conducting carbons. We also note here that the amount of SiO$_2$ in the C-PUA@silica-800 sample is ~25% (weight
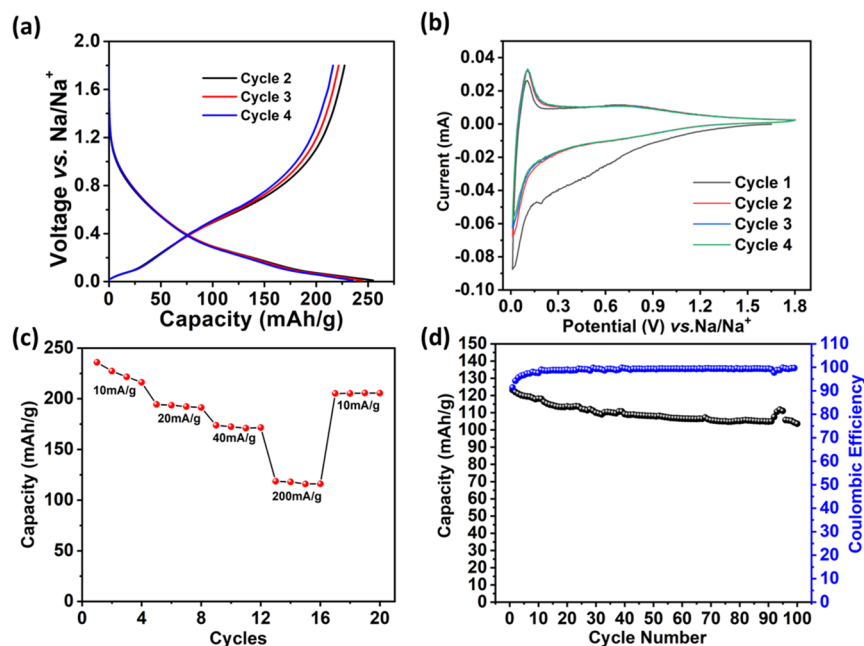
Figure 8. Electrochemical test done on the C-PUA@silica-800 sample without any incorporation of conductive carbon: (a) charge−discharge plot; (b) cyclic voltammetry; (c) rate capability; and (d) long cycle at a 200 mA/g current density.

percent) based on the TGA and EDS analysis,[47] which is a substantial amount of inactive material. Just considering the electrochemically active carbon materials without silica, the observed capacity would surpass 300 mAh/g (~316 mAh/g at a current density of 10 mA/g). Therefore, further optimization is needed to find the minimum amount of silica required to observe its positive role.

4. CONCLUSIONS

In summary, we demonstrated that C-PUA@silica-Temp xerogel powder-derived carbon aerogel-silica composites can be used for Na-ion anodes. All of the carbon aerogels synthesized at different temperatures show mesoporous structures and are active for Na-ion anodes with different capacities. Interestingly, the study shows that the mechanism of Na storage in the carbon aerogel can be different based on the temperature of pyrolysis. Therefore, the temperature of pyrolysis plays a crucial role in controlling the pore structures, the chemistry of pores, and their subsequent effect on achievable capacity and cycle life. Of the different carbon aerogels studied, 800 °C carbonized samples display good capacity and stable cycle life due to the beneficial role of embedded silica. It is anticipated that by varying the chemistry of parent xerogel precursors, the pore structures and pore surface areas can be controlled to obtain carbon aerogels in a sustainable way with optimized performance for Na-ion anodes.

ASSOCIATED CONTENT

ⓈⒾ Supporting Information

The Supporting Information is available free of charge at https://pubs.acs.org/doi/10.1021/acsaem.4c01769.

> Plots of IR spectra, Raman spectra, the specific capacity of samples, first-cycle Coulombic efficiency, capacity vs current density; electrochemical plots of first-cycle Coulombic efficiency, CV with higher scan rates, and capacity vs current density plot for each sample; charge—discharge plots of the C-PUA@silica-800 sample without conducting carbon, pure SiO_2, and SiC; and table of elemental compositional analysis from XPS spectra (PDF)

AUTHOR INFORMATION

Corresponding Authors

Chariklia Sotiriou-Leventis − *Department of Chemistry, Missouri S&T, Rolla, Missouri 65409, United States;* ⓘ orcid.org/0000-0003-3283-8257; Email: cslevent@mst.edu

Amitava Choudhury − *Department of Chemistry, Missouri S&T, Rolla, Missouri 65409, United States;* ⓘ orcid.org/0000-0001-5496-7346; Email: choudhurya@mst.edu

Authors

Santhoshkumar Sundaramoorthy − *Department of Chemistry, Missouri S&T, Rolla, Missouri 65409, United States;* ⓘ orcid.org/0000-0001-5037-0016

Rushi U. Soni − *Department of Chemistry, Missouri S&T, Rolla, Missouri 65409, United States;* ⓘ orcid.org/0000-0002-1855-8905

Stephen Yaw Owusu − *Department of Chemistry, Missouri S&T, Rolla, Missouri 65409, United States;* ⓘ orcid.org/0000-0002-5251-4287

Sutapa Bhattacharya − *Department of Chemistry, Missouri S&T, Rolla, Missouri 65409, United States;* ⓘ orcid.org/0000-0001-6591-6624

A. B. M. Shaheen ud Doulah − *Department of Chemistry, Missouri S&T, Rolla, Missouri 65409, United States;* ⓘ orcid.org/0000-0002-5413-0762

Vaibhav A. Edlabadkar − *Department of Chemistry, Missouri S&T, Rolla, Missouri 65409, United States;* ⓘ orcid.org/0000-0001-5763-7318

Complete contact information is available at:
https://pubs.acs.org/10.1021/acsaem.4c01769

Author Contributions

[†]S.S., R.U.S., and S.Y.O. contributed equally to this work.

Notes

The authors declare no competing financial interest.

REFERENCES

(1) Goodenough, J. B.; Park, K.-S. The Li-ion rechargeable battery: A perspective. *J. Am. Chem. Soc.* **2013**, *135* (4), 1167−1176.

(2) Tarascon, J.-M. Is lithium the new gold? *Nat. Chem.* **2010**, *2* (6), 510.

(3) Hirsh, H. S.; Li, Y.; Tan, D. H. S.; Zhang, M.; Zhao, E.; Meng, Y. S. Sodium-Ion Batteries Paving the Way for Grid Energy Storage. *Adv. Energy Mater.* **2020**, *10* (32), No. 2001274.

(4) Delmas, C. Sodium and Sodium-Ion Batteries: 50 Years of Research. *Adv. Energy Mater.* **2018**, *8* (17), No. 1703137.

(5) Goikolea, E.; Palomares, V.; Wang, S.; de Larramendi, I. R.; Guo, X.; Wang, G.; Rojo, T. Na-Ion Batteries—Approaching Old and New Challenges. *Adv. Energy Mater.* **2020**, *10* (44), No. 2002055.

(6) Dou, X.; Hasa, I.; Saurel, D.; Vaalma, C.; Wu, L.; Buchholz, D.; Bresser, D.; Komaba, S.; Passerini, S. Hard carbons for sodium-ion batteries: Structure, analysis, sustainability, and electrochemistry. *Mater. Today* **2019**, *23*, 87−104.

(7) Shao, W.; Shi, H.; Jian, X.; Wu, Z.-S.; Hu, F. Hard-Carbon Anodes for Sodium-Ion Batteries: Recent Status and Challenging Perspectives. *Adv. Energy Sustainability Res.* **2022**, *3* (7), No. 2200009.

(8) Stevens, D. A.; Dahn, J. R. In situ small-angle X-ray scattering study of sodium insertion into a nanoporous carbon anode material within an operating electrochemical cell. *J. Electrochem. Soc.* **2000**, *147* (12), 4428−4431.

(9) Stevens, D. A.; Dahn, J. R. The Mechanisms of Lithium and Sodium Insertion in Carbon Materials. *J. Electrochem. Soc.* **2001**, *148* (8), A803−A811.

(10) Anji Reddy, M.; Helen, M.; Groß, A.; Fichtner, M.; Euchner, H. Insight into Sodium Insertion and the Storage Mechanism in Hard Carbon. *ACS Energy Lett.* **2018**, *3* (12), 2851−2857.

(11) Matei Ghimbeu, C.; Górka, J.; Simone, V.; Simonin, L.; Martinet, S.; Vix-Guterl, C. Insights on the Na+ ion storage mechanism in hard carbon: Discrimination between the porosity, surface functional groups and defects. *Nano Energy* **2018**, *44*, 327−335.

(12) Au, H.; Alptekin, H.; Jensen, A. C. S.; Olsson, E.; O'Keefe, C. A.; Smith, T.; Crespo-Ribadeneyra, M.; Headen, T. F.; Grey, C. P.; Cai, Q.; Drew, A. J.; Titirici, M.-M. A revised mechanistic model for sodium insertion in hard carbons. *Energy Environ. Sci.* **2020**, *13* (10), 3469−3479.

(13) Yamamoto, H.; Muratsubaki, S.; Kubota, K.; Fukunishi, M.; Watanabe, H.; Kim, J.; Komaba, S. Synthesizing higher-capacity hard-

carbons from cellulose for Na- and K-ion batteries. *J. Mater. Chem. A* **2018**, *6* (35), 16844−16848.

(14) Qian, J.; Wu, F.; Ye, Y.; Zhang, M.; Huang, Y.; Xing, Y.; Qu, W.; Li, L.; Chen, R. Boosting Fast Sodium Storage of a Large-Scalable Carbon Anode with an Ultralong Cycle Life. *Adv. Energy Mater.* **2018**, *8* (16), No. 1703159.

(15) Meng, Q.; Lu, Y.; Ding, F.; Zhang, Q.; Chen, L.; Hu, Y.-S. Tuning the Closed Pore Structure of Hard Carbons with the Highest Na Storage Capacity. *ACS Energy Lett.* **2019**, *4* (11), 2608−2612.

(16) Zhang, G.; Zhang, L.; Ren, Q.; Yan, L.; Zhang, F.; Lv, W.; Shi, Z. Tailoring a Phenolic Resin Precursor by Facile Pre-oxidation Tactics to Realize a High-Initial-Coulombic-Efficiency Hard Carbon Anode for Sodium-Ion Batteries. *ACS Appl. Mater. Interfaces* **2021**, *13* (27), 31650−31659.

(17) Song, M.; Yi, Z.; Xu, R.; Chen, J.; Cheng, J.; Wang, Z.; Liu, Q.; Guo, Q.; Xie, L.; Chen, C. Towards enhanced sodium storage of hard carbon anodes: Regulating the oxygen content in precursor by low-temperature hydrogen reduction. *Energy Storage Materials* **2022**, *51*, 620−629.

(18) Chen, X.; Sawut, N.; Chen, K.; Li, H.; Zhang, J.; Wang, Z.; Yang, M.; Tang, G.; Ai, X.; Yang, H.; Fang, Y.; Cao, Y. Filling carbon: a microstructure-engineered hard carbon for efficient alkali metal ion storage. *Energy Environ. Sci.* **2023**, *16* (9), 4041−4053.

(19) Song, Z.; Li, F.; Mao, L.; Lin, W.; Zheng, L.; Huang, Y.; Wei, M.; Hong, Z. Sustainable Fabrication of a Practical Hard Carbon Anode for a Sodium-Ion Battery with Unprecedented Long Cycle Life. *ACS Sustainable Chem. Eng.* **2023**, *11* (41), 5020−15030.

(20) Hou, Z.; Lei, D.; Jiang, M.; Gao, Y.; Zhang, X.; Zhang, Y.; Wang, J.-G. Biomass-Derived Hard Carbon with Interlayer Spacing Optimization toward Ultrastable Na-Ion Storage. *ACS Appl. Mater. Interfaces* **2023**, *15* (1), 1367−1375.

(21) Sun, Y.; Hou, R.; Xu, S.; Zhou, H.; Guo, S. Molecular Engineering Enabling High Initial Coulombic Efficiency and Robust Solid Electrolyte Interphase for Hard Carbon in Sodium-Ion Batteries. *Angew. Chem., Int. Ed.* **2024**, *63*, No. e202318960.

(22) Jin, Y.; Sun, S.; Ou, M.; Liu, Y.; Fan, C.; Sun, X.; Peng, J.; Li, Y.; Qiu, Y.; Wei, P.; Deng, Z.; Xu, Y.; Han, J.; Huang, Y. High-Performance Hard Carbon Anode: Tunable Local Structures and Sodium Storage Mechanism. *ACS Appl. Energy Mater.* **2018**, *1* (5), 2295−2305.

(23) Li, Z.; Ma, L.; Surta, T. W.; Bommier, C.; Jian, Z.; Xing, Z.; Stickle, W. F.; Dolgos, M.; Amine, K.; Lu, J.; Wu, T.; Ji, X. High Capacity of Hard Carbon Anode in Na-Ion Batteries Unlocked by POx Doping. *ACS Energy Lett.* **2016**, *1* (2), 395−401.

(24) Zhou, C.; Wang, D.; Li, A.; Pan, E.; Liu, H.; Chen, X.; Jia, M.; Song, H. Three-dimensional porous carbon doped with N, O and P heteroatoms as high-performance anode materials for sodium ion batteries. *Chem. Eng. J.* **2020**, *380*, No. 122457.

(25) Sun, N.; Zhao, R.; Xu, M.; Zhang, S.; Soomro, R. A.; Xu, B. Design advanced nitrogen/oxygen co-doped hard carbon microspheres from phenolic resin with boosted Na-storage performance. *J. Power Sources* **2023**, *564*, No. 232879.

(26) Wang, H.-L.; Shi, Z.-Q.; Jin, J.; Chong, C.-B.; Wang, C.-Y. Properties and sodium insertion behavior of Phenolic Resin-based hard carbon microspheres obtained by a hydrothermal method. *J. Electroanal. Chem.* **2015**, *755*, 87−91.

(27) Fan, C.; Zhang, R.; Luo, X.; Hu, Z.; Zhou, W.; Zhang, W.; Liu, J.; Liu, J. Epoxy phenol novolac resin: A novel precursor to construct high performance hard carbon anode toward enhanced sodium-ion batteries. *Carbon* **2023**, *205*, 353−364.

(28) Xiao, L.; Cao, Y.; Henderson, W. A.; Sushko, M. L.; Shao, Y.; Xiao, J.; Wang, W.; Engelhard, M. H.; Nie, Z.; Liu, J. Hard carbon nanoparticles as high-capacity, high-stability anodic materials for Na-ion batteries. *Nano Energy* **2016**, *19*, 279−288.

(29) Rao, X.; Lou, Y.; Chen, J.; Lu, H.; Cheng, B.; Wang, W.; Fang, H.; Li, H.; Zhong, S. Polyacrylonitrile Hard Carbon as Anode of High Rate Capability for Lithium Ion Batteries. *Front. Energy Res.* **2020**, *8*, 3.

(30) Jin, J.; Yu, B.-J.; Shi, Z.-Q.; Wang, C.-Y.; Chong, C.-B. Lignin-based electrospun carbon nanofibrous webs as free-standing and binder-free electrodes for sodium ion batteries. *J. Power Sources* **2014**, *272*, 800−807.

(31) Jiang, Q.; Zhang, Z.; Yin, S.; Guo, Z.; Wang, S.; Feng, C. Biomass carbon micro/nano-structures derived from ramie fibers and corncobs as anode materials for lithium-ion and sodium-ion batteries. *Appl. Surf. Sci.* **2016**, *379*, 73−82.

(32) Dou, X.; Hasa, I.; Saurel, D.; Jauregui, M.; Buchholz, D.; Rojo, T.; Passerini, S. Impact of the Acid Treatment on Lignocellulosic Biomass Hard Carbon for Sodium-Ion Battery Anodes. *ChemSusChem* **2018**, *11* (18), 3276−3285.

(33) Escamilla-Pérez, A. M.; Beda, A.; Simonin, L.; Grapotte, M.-L.; Le-Meins, J. M.; Matei Ghimbeu, C. Biopolymer-Based Hard Carbons: Correlations between Properties and Performance as a Na-Ion Battery Anode. *ACS Appl. Energy Mater.* **2023**, *6* (14), 7419−7432.

(34) Hong, K.-L.; Qie, L.; Zeng, R.; Yi, Z.-Q.; Zhang, W.; Wang, D.; Yin, W.; Wu, C.; Fan, Q.-J.; Zhang, W.-X.; Huang, Y.-H. Biomass derived hard carbon used as a high performance anode material for sodium ion batteries. *J. Mater. Chem. A* **2014**, *2* (32), 12733−12738.

(35) Liu, P.; Li, Y.; Hu, Y.-S.; Li, H.; Chen, L.; Huang, X. A waste biomass derived hard carbon as a high-performance anode material for sodium-ion batteries. *J. Mater. Chem. A* **2016**, *4* (34), 13046−13052.

(36) Thompson, M.; Xia, Q.; Hu, Z.; Zhao, X. S. A review on biomass-derived hard carbon materials for sodium-ion batteries. *Mater. Adv.* **2021**, *2* (18), 5881−5905.

(37) Kumar, U.; Goonetilleke, D.; Gaikwad, V.; Pramudita, J. C.; Joshi, R. K.; Sharma, N.; Sahajwalla, V. Activated Carbon from E-Waste Plastics as a Promising Anode for Sodium-Ion Batteries. *ACS Sustainable Chem. Eng.* **2019**, *7* (12), 10310−10322.

(38) Fonseca, W. S.; Meng, X.; Deng, D. Trash to Treasure: Transforming Waste Polystyrene Cups into Negative Electrode Materials for Sodium Ion Batteries. *ACS Sustainable Chem. Eng.* **2015**, *3* (9), 2153−2159.

(39) Nagmani, P. S. Utilization of PET derived hard carbon as a battery-type, higher plateau capacity anode for sodium-ion and potassium-ion batteries. *J. Electroanal. Chem.* **2023**, *946*, No. 117731.

(40) Far, H. M.; Donthula, S.; Taghvaee, T.; Saeed, A. M.; Garr, Z.; Sotiriou-Leventis, C.; Leventis, N. Air-Oxidation of Phenolic Resin Aerogels: Backbone Reorganization, Formation of Ring-Fused Pyrylium Cations, and the Effect on Microporous Carbons with Enhanced Surface Areas. *RSC Adv.* **2017**, *7*, 51104−51120.

(41) Saeed, A. M.; Rewatkar, P. M.; Majedi Far, H.; Taghvaee, T.; Donthula, S.; Mandal, C.; Sotiriou-Leventis, C.; Leventis, N. Selective CO2 Sequestration with Monolithic Bimodal Micro/Macroporous Carbon Aerogels Derived from Stepwise Pyrolytic Decomposition of Polyamide-Polyimide-Polyurea Random Copolymers. *ACS Appl. Mater. Interfaces* **2017**, *9*, 13520−13536.

(42) Sadekar, A. G.; Mahadik, S. S.; Bang, A. N.; Larimore, Z. J.; Wisner, C. A.; Bertino, M. F.; Kalkan, A. K.; Mang, J. T.; Sotiriou-Leventis, C.; Leventis, N. From "Green" Aerogels to Porous Graphite by Emulsion Gelation of Acrylonitrile. *Chem. Mater.* **2012**, *24*, 26−47.

(43) Mahadik-Khanolkar, S.; Donthula, S.; Sotiriou-Leventis, C.; Leventis, N. Polybenzoxazine Aerogels. 1. High-Yield Room-Temperature Acid-Catalyzed Synthesis of Robust Monoliths, Oxidative Aromatization, and Conversion to Microporous Carbons. *Chem. Mater.* **2014**, *26*, 1303−1317.

(44) Lee, J.-H.; Park, S.-J. Recent advances in preparations and applications of carbon aerogels: A review. *Carbon* **2020**, *163*, 1−18.

(45) Chen, Y.; Zhang, Z.; Lai, Y.; Shi, X.; Li, J.; Chen, X.; Zhang, K.; Li, J. Self-assembly of 3D neat porous carbon aerogels with NaCl as template and flux for sodium-ion batteries. *J. Power Sources* **2017**, *359*, 529−538.

(46) Melzi d'Eril, M.; Zambotti, A.; Graczyk-Zajac, M.; Ionescu, E.; Sorarù, G. D.; Riedel, R. Effect of ultra-fast pyrolysis on polymer-derived SiOC aerogels and their application as anodes for Na-ion batteries. *Open Ceramics* **2023**, *14*, No. 100354.

(47) Soni, R. U.; Edlabadkar, V. A.; Greenan, D.; Rewatkar, P. M.; Leventis, N.; Sotiriou-Leventis, C. Preparation of Carbon Aerogels from Polymer-Cross-Linked Xerogel Powders without Supercritical Fluid Drying and Their Application in Highly Selective CO2Adsorption. *Chem. Mater.* **2022**, *34* (11), 4828−4847.

(48) Leventis, N.; Elder, I. A.; Rolison, D. R.; Anderson, M. L.; Merzbacher, C. I. Durable Modification of Silica Aerogel Monoliths with Fluorescent 2,7-Diazapyrenium Moieties. Sensing Oxygen near the Speed of Open-Air Diffusion. *Chem. Mater.* **1999**, *11*, 2837−2845.

(49) Rewatkar, P. M.; Taghvaee, T.; Saeed, A. M.; Donthula, S.; Mandal, C.; Chandrasekaran, N.; Leventis, T.; Shruthi, T. K.; Sotiriou-Leventis, C.; Leventis, N. Sturdy, Monolithic SiC and Si_3N_4 Aerogels from Compressed Polymer-Cross-Linked Silica Xerogel Powders. *Chem. Mater.* **2018**, *30*, 1635−1647.

(50) Leventis, N. Three-Dimensional Core-Shell Superstructures: Mechanically Strong Aerogels. *Acc. Chem. Res.* **2007**, *40*, 874−884.

(51) Feller, T.; Rosenfeldt, S.; Retsch, M. Carbothermal synthesis of micron-sized, uniform, spherical silicon carbide (SiC) particles. *Z. Anorg. Allg. Chem.* **2021**, *647*, 2172−2180.

(52) Guo, J.; Song, K.; Wu, B.; Zhu, X.; Zhang, B.; Shi, Y. Atomically thin SiC nanoparticles obtained: Via ultrasonic treatment to realize enhanced catalytic activity for the oxygen reduction reaction in both alkaline and acidic media. *RSC Adv.* **2017**, *7* (37), 22875−22881.

(53) Kaspar, J.; Storch, M.; Schitco, C.; Riedel, R.; Graczyk-Zajacz, M. SiOC(N)/hard carbon composite anodes for Na-ion batteries: Influence of morphology on the electrochemical properties. *J. Electrochem. Soc.* **2016**, *163* (2), A156−A162.

(54) Edlabadkar, V. A.; Soni, R. U.; Doulah, ABM.S.; Owusu, S. Y.; Hackett, S.; Bartels, J. M.; Leventis, N.; Sotiriou-Leventis, C. CO_2 Uptake by Microporous Carbon Aerogels Derived from Polybenzoxazine and Analogous All-Nitrogen Polybenzodiazine Aerogels. *Chem. Mater.* **2024**, *3*, 1172−1187.

(55) Dong, Y.; Zhang, S.; Du, X.; Hong, S.; Zhao, S.; Chen, Y.; Chen, X.; Song, H. Boosting the Electrical Double-Layer Capacitance of Graphene by Self-Doped Defects through Ball-Milling. *Adv. Funct. Mater.* **2019**, *29* (24), No. 1901127.

(56) Bechelany, M.; Brioude, A.; Cornu, D.; Ferro, G.; Miele, P. A Raman spectroscopy study of individual SiC nanowires. *Adv. Funct. Mater.* **2007**, *17* (6), 939−943.

(57) Chikvaidze, G.; Mironova-Ulmane, N.; Plaude, A.; Sergeev, O. Investigation of silicon carbide polytypes by Raman spectroscopy. *Latv. J. Phys. Technol. Sci.* **2014**, *51* (3), 51−57.